Journal of Medical Imaging

MedicalImaging.SPIEDigitalLibrary.org

Task-driven source–detector trajectories in cone-beam computed tomography: II. Application to neuroradiology

Sarah Capostagno
J. Webster Stayman
Matthew Jacobson
Tina Ehtiati
Clifford R. Weiss
Jeffrey H. Siewerdsen

SPIE.

Sarah Capostagno, J. Webster Stayman, Matthew Jacobson, Tina Ehtiati, Clifford R. Weiss, Jeffrey H. Siewerdsen, "Task-driven source–detector trajectories in cone-beam computed tomography: II. Application to neuroradiology," *J. Med. Imag.* **6**(2), 025004 (2019), doi: 10.1117/1.JMI.6.2.025004.

Task-driven source–detector trajectories in cone-beam computed tomography: II. Application to neuroradiology

Sarah Capostagno,[a,†] J. Webster Stayman,[a,†] Matthew Jacobson,[a] Tina Ehtiati,[b] Clifford R. Weiss,[a,c] and Jeffrey H. Siewerdsen[a,c,*]
[a]Johns Hopkins University, Department of Biomedical Engineering, Baltimore, Maryland, United States
[b]Siemens Medical Solutions USA, Inc., Imaging and Therapy Systems, Hoffman Estates, Illinois, United States
[c]Johns Hopkins University, Department of Radiology and Radiological Science, Baltimore, Maryland, United States

Abstract. We apply the methodology detailed in "Task-driven source–detector trajectories in cone-beam computed tomography: I. Theory and methods" by Stayman *et al.* for task-driven optimization of source–detector orbits in cone-beam computed tomography (CBCT) to scenarios emulating imaging tasks in interventional neuroradiology. The task-driven imaging framework is used to optimize the CBCT source–detector trajectory by maximizing the detectability index, d'. The approach was applied to simulated cases of endovascular embolization of an aneurysm and arteriovenous malformation and was translated to real data first using a CBCT test bench followed by implementation on an interventional robotic C-arm. Task-driven trajectories were found to generally favor higher fidelity (i.e., less noisy) views, with an average increase in d' ranging from 7% to 28%. Visually, this resulted in improved conspicuity of particular stimuli by reducing the noise and altering the noise correlation to a form distinct from the spatial frequencies associated with the imaging task. The improvements in detectability and the demonstration of the task-driven workflow using a real interventional imaging system show the potential of the task-driven imaging framework to improve imaging performance on motorized, multiaxis C-arms in neuroradiology. [DOI: 10.1117/1.JMI.6.2.025004]

Keywords: task-driven imaging; cone-beam computed tomography; robotic C-arm; imaging task; detectability index; task function; model-based image reconstruction; optimization; image quality; interventional imaging; neuroradiology.

Paper 18252R received Nov. 20, 2018; accepted for publication Apr. 4, 2019; published online May 9, 2019.

1 Introduction

Cone-beam computed tomography (CBCT) is used in a growing number of scenarios in interventional imaging, including verification of patient positioning, three-dimensional (3-D) image guidance, and visualization of instrumentation or embolic agents delivered to the patient.[1,2] Robotic CBCT C-arms greatly expand the scanning geometries possible beyond the conventional circular source–detector orbits. In clinical practice, such motion capabilities have been used to provide fast, reproducible positioning of the C-arm gantry and to increase the field of view (FOV) of the reconstructed 3-D image. As demonstrated in the work reported below, the additional degrees of freedom (DoFs) enabled by such robotic C-arm gantries can be leveraged to improve image quality and/or reduce the radiation dose using noncircular orbits computed to maximize the imaging performance with respect to a particular imaging task (or tasks).

As discussed in the corresponding paper[3] titled, "Task-driven source–detector trajectories in cone-beam computed tomography: I. Theory and methods," CBCT-guided interventional procedures often include a considerable amount of information regarding patient-specific anatomy and the imaging task (or tasks). As shown in Refs. 4–7, the definition of the imaging task and a patient-specific prior image can be used to optimize both the acquisition and the reconstruction of CBCT image data. Such prospective design of the CBCT scan technique and/or reconstruction method based on a task-based objective function is referred to as task-driven imaging. In this paper, we focus on the task-driven design of the CBCT source–detector trajectory, taking the mathematical theory and methods detailed in Ref. 3 and applying them to scenarios emulating neurosurgical/neuroradiological interventions.

One example clinical scenario in which task-driven imaging could be applied is neurovascular embolization, which may be performed in response to a cerebral aneurysm, arteriovenous malformation (AVM), carotid-cavernous fistula, or dural arteriovenous fistula.[8] The embolization agent occludes feeder vessels and vascular abnormalities, and during the procedure it is important to avoid embolization of normal/nontarget vessels, identify incomplete embolization, and locate possible hemorrhage resulting from perforated vessels.[9] CBCT is frequently used as a tool to localize the target and instrumentation as well as to check against possible complications arising from the intervention. However, image quality is often degraded by the presence of materials that are highly attenuating to x-rays including coils, plugs, balloons, particulate agents such as polyvinyl alcohol and microspheres, and liquids such as tissue adhesives and Onyx systems.[10] As a result, CBCT images often exhibit strong artifacts that challenge reliable visualization of the target and surrounding vessels.

In this work, we apply task-driven imaging to two clinical scenarios: the assessment of embolization in the case of aneurysm, where perforation of the aneurysm would necessitate detection of intracranial hemorrhage adjacent to the region of

*Address all correspondence to Jeffrey H. Siewerdsen, E-mail: jeff.siewerdsen@jhu.edu

†Sarah Capostagno and J. Webster Stayman contributed equally to this work.

2329-4302/2019/$25.00 © 2019 SPIE

embolization; and AVM ablation, where detection of untreated regions of the nidus requires visualization of incomplete embolization. We investigate these two scenarios both in simulation and in real data using a CBCT test bench and a clinical robotic C-arm, and extend the framework to situations for which multiple tasks with unknown location underlie the clinical objective.

A potential clinical workflow is depicted in Fig. 1 for practical application of task-driven imaging to image-guided neurovascular interventions. The process begins with some form of prior 3-D image as a model of the patient (μ_{prior}). This could be a multidetector CT acquired for diagnostic or planning purposes or an initial CBCT acquired at the beginning of the case for navigation or target localization. Based on the expected surgical outcome of the procedure, high-contrast features are added to the anatomical model (e.g., embolization coils and contrast agent). The imaging tasks are defined mathematically in $H_{\text{Task}(j)}$ with their locations (j_{ROI}) specified within a region of interest in μ_{prior}. Note that the coordinate system of μ_{prior} must be registered to the world coordinate system of the intraoperative scene – i.e., to the C-arm gantry. To accomplish this, two or more projections are acquired, and the registration of the prior 3-D image and intraoperative scene is solved via 3-D to 2-D registration, as shown in Ref. 11. The resulting six DoF transformation $T^{C-\text{arm}}_{\mu_{\text{prior}}}$ (containing three rotations and three translations in x, y, and z) can be applied to the image coordinates of μ_{prior} to yield transformed coordinates registered to the C-arm gantry. Maximization of task-based detectability index (d') is solved with respect to the source–detector orbit (parametrized by Ω) to yield the optimal source–detector trajectory $\hat{\Omega}$. An important consideration is the need for a geometric calibration to precisely characterize the source and detector pose for each vertex on the resulting orbit. Even conventional circular orbits require such calibration to obtain accurate 3-D reconstruction, usually solved by prior (offline) calibration techniques using a phantom of fiducial markers.[12–14] Offline calibration of the full range of possible vertices may or may not be practical; however, a solution can also be obtained using the "self-calibration" method described in Ref. 15. Model-based image reconstruction can then be utilized to reconstruct the acquired task-driven image $\hat{\mu}$. The mathematical details of task-driven imaging for source–detector trajectory optimization are discussed in Sec. 2.

2 Task-Driven Imaging for Design of Source–Detector Trajectories

The companion paper[3] provides an in-depth description of the theoretical methods of trajectory design in task-driven imaging which is briefly reviewed here. Task-driven imaging is an imaging framework well suited for image-guided interventions (IGIs), in which a preoperative 3-D image is acquired for diagnostic or planning purposes—or alternatively, in which multiple 3-D images are acquired during the course of the intervention. We leverage the prior 3-D image to define the imaging task in terms of both the patient-specific anatomy and the clinical objective of an intraoperative CBCT scan. For example, after an interventional embolization of a neurovascular target, the imaging task may be to detect a subtle, low-contrast hemorrhage adjacent to the high-contrast embolization coil.

The imaging task can be defined mathematically according to the location, contrast, and spatial frequencies associated with the feature of interest. Imaging performance is optimized with respect to the task ($H_{\text{Task}(j)}$, with subscript j marking the location of interest) by maximizing the detectability index d'_j, which in turn is determined by the noise-power spectrum NPS_j and modulation transfer function MTF_j. The nonprewhitening observer model for detectability is given as

$$d'^2_j(\Omega) = \frac{\left\{\iiint [\text{MTF}_j(\Omega)\cdot H_{\text{Task}(j)}]^2 \text{d}f_x\,\text{d}f_y\,\text{d}f_z\right\}^2}{\iiint \text{NPS}_j(\Omega)\cdot[\text{MTF}_j(\Omega)\cdot H_{\text{Task}(j)}]^2 \text{d}f_x\,\text{d}f_y\,\text{d}f_z}, \tag{1}$$

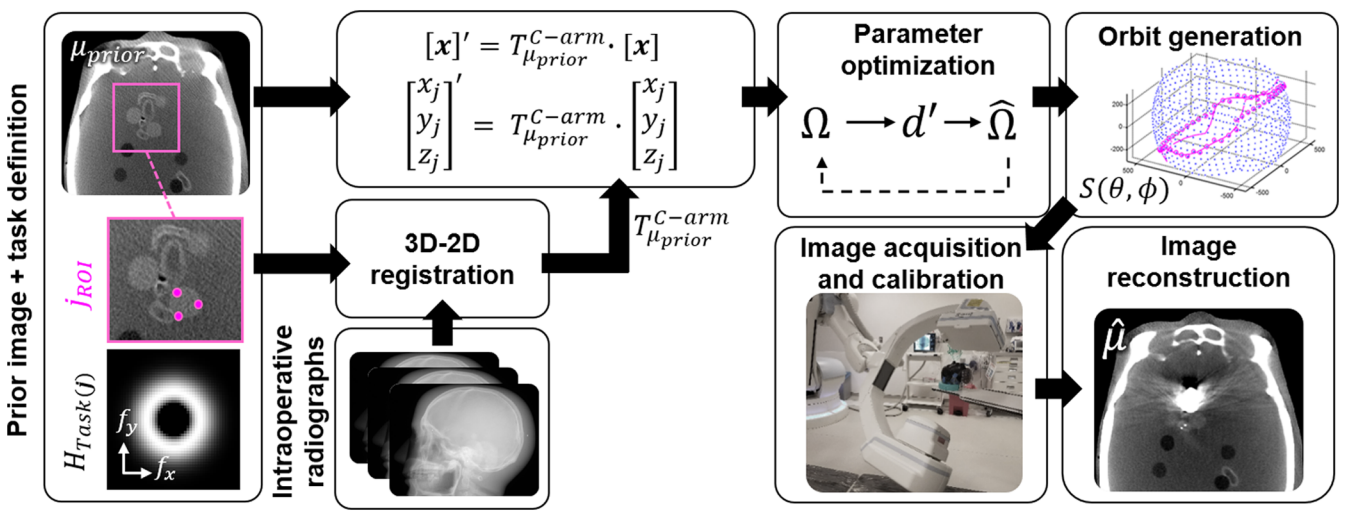

Fig. 1 Workflow for task-driven imaging. A prior 3-D image provides a patient model within which the imaging tasks are defined. The coordinates of the prior image and task locations (x and j, respectively) are mapped to the coordinate system of the imaging system using the six DoF transform $T^{C-\text{arm}}_{\mu_{\text{prior}}}$, which is solved by 3-D–2-D registration of μ_{prior} to two or more projection views, yielding the transformed coordinates in x' and j'. Optimization of Ω with respect to detectability (d') yields a task- and patient-specific trajectory $S(\theta, \phi)$, which is carried out on the robotic C-arm and reconstructed using model-based image reconstruction.

where Ω is a vector containing parameters that generally characterize the CBCT scan—e.g., beam energy, fluence (as in Ref. 16), or reconstruction filters or regularization (as in Ref. 17), and f_i indicates the spatial frequencies in the three cardinal directions of the image coordinate system ($i \in [x, y, z]$). The nonprewhitening observer model is advantageous in that it combines $H_{\text{Task}(j)}$ with the relevant (and predictable) properties of the image, allowing the detection of objects ranging from low frequency (i.e., diffuse lesion) to high frequency (i.e., stents, small vessels, etc.). Other metrics can be envisioned (e.g., contrast-to-noise ratio, which considers only low-frequency transfer characteristics), and other forms of the observer model could be formulated to incorporate an imaging task with predictions of image properties. In addition, incorporating other technical, logistic factors such as scan time, dose, or total number of views could be beneficial for workflow in the clinical setting.

In this work Ω comprises parameters that define the source–detector trajectory. This parameterization can take a variety of forms, including periodic basis functions using constant, sine, and cosine functions, and B-spline basis functions using equally spaced knot locations, as described in Ref. 3. Calculation of NPS_j and MTF_j uses approximations based on penalized-likelihood (PL) reconstruction with a quadratic regularization penalty,[18] which is also detailed in Ref. 3.

Through NPS_j and MTF_j, the optimization of Ω yields an orbit that maximizes d'_j with respect to $H_{\text{Task}(j)}$. As discussed in Ref. 3, it may be useful to optimize with respect to multiple task locations (e.g., when a single location is unknown). For the experiments presented below in which all locations are treated with equal importance, we have chosen to maximize the minimum d'_j according to

$$\hat{\Omega} = \text{argmax}_{\Omega}\, \text{minimum}\{d'^2_1[\Omega; H_{\text{Task}(1)}], d'^2_2[\Omega; H_{\text{Task}(2)}], \ldots, d'^2_L[\Omega; H_{\text{Task}(L)}]\}. \quad (2)$$

Using the maxi-min objective better ensures that imaging performance is not sacrificed in some locations in favor of others, recognizing that other objectives may be used. These can include maxi-mean or maxi-median (also explored in Ref. 3), a weighted sum when additional knowledge of the importance of each defined task is available, or another relevant statistical representation of a population.

We solve the optimization using the covariance matrix adaptation-evolution strategy (CMA-ES[19])—a stochastic optimization that has been previously shown to perform well in the presence of local minima.[20] Once the optimal parameters are found ($\hat{\Omega}$), the low-dimensional parametrization of the source–detector trajectory can be converted into a series of source locations $[S_n(\theta, \phi);\ n = 1, \ldots, N]$ using a rotation angle (θ) and a tilt angle (ϕ) to indicate the 3-D location of the x-ray source for all N projections in the scan. In the current work, we assume that the position of the detector is fixed with respect to the x-ray source (fixed source–detector distance, SDD) and that there is a single, fixed origin, allowing the source–detector trajectory to move on a sphere of diameter SDD.

For image reconstruction, we use the PL reconstruction algorithm as such iterative methods naturally accommodate the noncircular trajectories generated by task-driven imaging. The PL algorithm maximizes an objective function based on the log-likelihood L of the current image estimate μ (given the projection data y) combined with a regularization term to enforce smoothness in the image with regularization strength β

$$\hat{\mu} = \text{argmax}_{\mu}\, \text{L}(\mu; y) - \beta R(\mu). \quad (3)$$

We use a quadratic penalty for the regularization term $R(\mu)$, matching the theoretical estimators for NPS_j and MTF_j, as discussed in Ref. 3.

3 Experimental Methods

3.1 *Experimental Imaging Systems and Digital Simulation*

Studies included a combination of simulation and physical experiments. The first experimental system was a CBCT test bench, as shown in Fig. 2(a), allowing a broad range of trajectories by combining a motorized rotation stage with a manual tilt platform. The second system was a robotic C-arm (Artis Zeego, Siemens Healthineers, Forcheim Germany), as shown in Fig. 2(b). Each system permitted task-driven scans in which

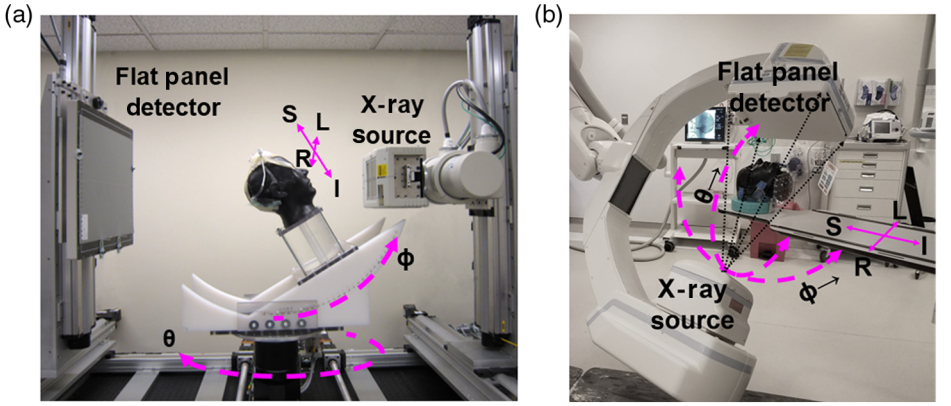

Fig. 2 Experimental platforms for task-driven imaging. (a) CBCT test bench with rotational platform and manual tilt stage. (b) The robotic C-arm system. In each system, the source–detector trajectory is defined by a series of N source locations containing two DoFs: rotation angle θ and tilt angle ϕ. The patient's right (R), left (L), superior (S), and inferior (I) directions are indicated in the rotating coordinate frame of the patient on the test bench and in the world reference frame for the C-arm.

the x-ray source moved (either in a true world-frame orbit for the robotic C-arm or relative to the patient for the test bench) to each $S_n(\theta,\phi)$ in $S(\theta,\phi)$ in a step-and-shoot fashion to accumulate the N projections constituting the task-driven sinogram. To accomplish this, each source location generated by the task-driven orbit was defined using two DoF; a rotational angle (θ) and a tilt angle (ϕ) for all N source locations.

For the test bench system, scans were performed at 100 kV (with 2.0 mm Al + 0.2 mm Cu added filtration) and 0.63 mAs per projection. System geometry was set to 120 cm source-to-detector distance and 60 cm source-to-axis distance, and the detector was read at 768×768 pixel format with 0.556 mm^2 pixels. A fairly complete sampling of vertices was obtained by a combination of rotations (1 deg to 360 deg in 1 deg increments of the rotation stage, equivalent to source–detector rotation) and tilts (−30 deg to +30 deg in 2.5 deg increments of a tilt platform, equivalent to source–detector tilt). As the tilt platform was placed on top of the rotary stage [as in Fig. 2(a)], this yields an incomplete sampling pattern, particularly in the direction orthogonal to the tilt platform; therefore, the tilt platform was also physically rotated by 90 deg on the rotation axis for additional coverage of the sphere. From each circular scan, 182 samples were used, giving 10,556 vertices in total (182 views × 2 tilt platform orientations × 29 tilt angles). Geometric calibration of each 360-deg orbit was performed using a BB phantom and the method described in Ref. 13. Task-driven orbits were formed by selecting 364 vertices from this set of projection data as nearest match to the solution of Eq. (2). The scan dose was evaluated by measuring the air kerma using a 0.6-cc air ionization chamber placed within a 16-cm diameter CTDI phantom at isocenter[21,22] and computing the weighted sum (denoted by D_w, given by the 1/3 and 2/3 weighted sum of the central and average peripheral doses, respectively).

For the robotic C-arm platform, system geometry was set to 120 cm source-to-detector distance and 80-cm source-to-axis distance, and the detector was read at 960×1240 pixel format with 0.308×0.308-mm^2 pixels. Rotation and tilt parameters for the C-arm gantry were uploaded to the Artis control system as an XML file, and individual projections were acquired at 102 kV and 0.18 mAs per projection to avoid saturation of the detector with automatic exposure control disabled and no added filtration, resulting in 63 mAs total for the scan. Raw projection data were collected using an engineering workstation, and the self-calibration method was used for geometric calibration,[15] as only vertices belonging to noncircular orbits were collected (cf., full sampling of vertices on the test bench).

The following sections outline the experiments demonstrating the method as applied to neurointerventional radiology. First, we simulated embolization of an intracranial aneurysm in a digital anthropomorphic head phantom to demonstrate the use of a multitask objective function, progressing from non-anthropomorphic phantoms in Ref. 3. We then used the above-described CBCT test bench to test the embolization scenario in real data. Next, we digitally simulated AVM embolization to show the effect of surrounding anatomy on optimal orbits by moving the location of stimuli within the (digital) cranium and repeating the task-driven optimization. Finally, we implemented the above-described task-driven imaging framework on the robotic C-arm system to demonstrate the task-driven source–detector trajectories computed and exercised on a real clinical system.

3.2 *Multitask Optimization*

The first experiment emulated the assessment of an intracranial aneurysm coil embolization. Postoperative CT or CBCT is commonly used to check for complications in the coil, including perforation of the aneurysm and associated hemorrhage. A digital anthropomorphic head phantom was created with a centrally located, coiled aneurysm [Fig. 3(a)]. The embolization coil was modeled as a rough ellipsoid with principal axes of $20\times12\times13$ mm^3 and attenuation coefficient (μ) of 0.8 mm^{-1} (corresponding to ∼8% filling by volume of platinum wire using an x-ray beam with 90 kVp peak energy). Six 11-mm diameter spheres were placed around the coil, representing the intracranial hemorrhage with a contrast of 0.002 mm^{-1} relative to background (similar to fresh blood in brain). Simulations used a monoenergetic forward model with added Poisson noise and the test bench geometry, which were described in Sec. 3.1, with uniform sampling in θ from 1 deg to 360 deg and uniform sampling in ϕ from −50 deg to +50 deg (in 1 deg increments). Bare-beam fluence was modeled with 10^5 photons per detector element approximating an exposure of 85 mAs with a beam energy of 90 kV.

The task function corresponding to the 11-mm spherical hemorrhage is shown in Fig. 3(e). A low-frequency task function was chosen for detecting the low-contrast, diffuse hemorrhage and a maxi-min, multilocation objective was solved with 30 locations surrounding the embolization coil using the on-the-fly computation approach, as described in Ref. 3. The locations were uniformly distributed over an ellipsoid around the coil with principal axes of $36\times24\times24$ mm^3. The source–detector orbit was parameterized using nine periodic basis functions with ϕ constrained to ±50 deg. The CMA-ES algorithm was applied using a population size of 40 and five initializations corresponding to circular orbits with $\phi=\{-50\ \text{deg}, -25\ \text{deg}, 0\ \text{deg}, 25\ \text{deg}, 50\ \text{deg}\}$. The solution with the highest maxi-min detectability was chosen and compared with a standard circular orbit using the same number of projections and bare-beam fluence (exposure). Image reconstruction for both the task-driven orbit and reference circular orbit solved the PL objective using dynamically relaxed ordered subsets with the number of subsets decreasing every five iterations in the sequence $\{54, 24, 12, 6, 4, 2, 1\}$ for a total of 50 iterations to accelerate convergence. Quadratic regularization strength with $\beta=10^5$ was manually selected to balance the trade-off between noise and resolution, and the 3-D image was reconstructed with $480\times480\times500$ voxels with 0.5-mm^3 voxels.

3.3 *Task-Driven Imaging in Real Data (CBCT Test Bench)*

An initial physical experiment used the CBCT test bench to further investigate the embolization scenario described in Sec. 3.2. In this case, a custom anthropomorphic phantom (The Phantom Laboratory, Greenwich, New York) was used with a human skull surrounded by tissue-equivalent plastic with the cranial vault filled with brain-equivalent gelatin ($\mu=0.0188$ mm^{-1}). A silicone vessel (Vascular Simulations, Stony Brook, New York) representing an intracranial aneurysm in the internal carotid artery was placed in the interior of the cranium. Four 12.7-mm diameter acrylic spheres ($\mu=0.0195$ mm^{-1}) were attached to the external surface of the aneurysm to simulate intracranial hemorrhage, as illustrated in Fig. 3(b). An initial CBCT scan was acquired to provide a preoperative image

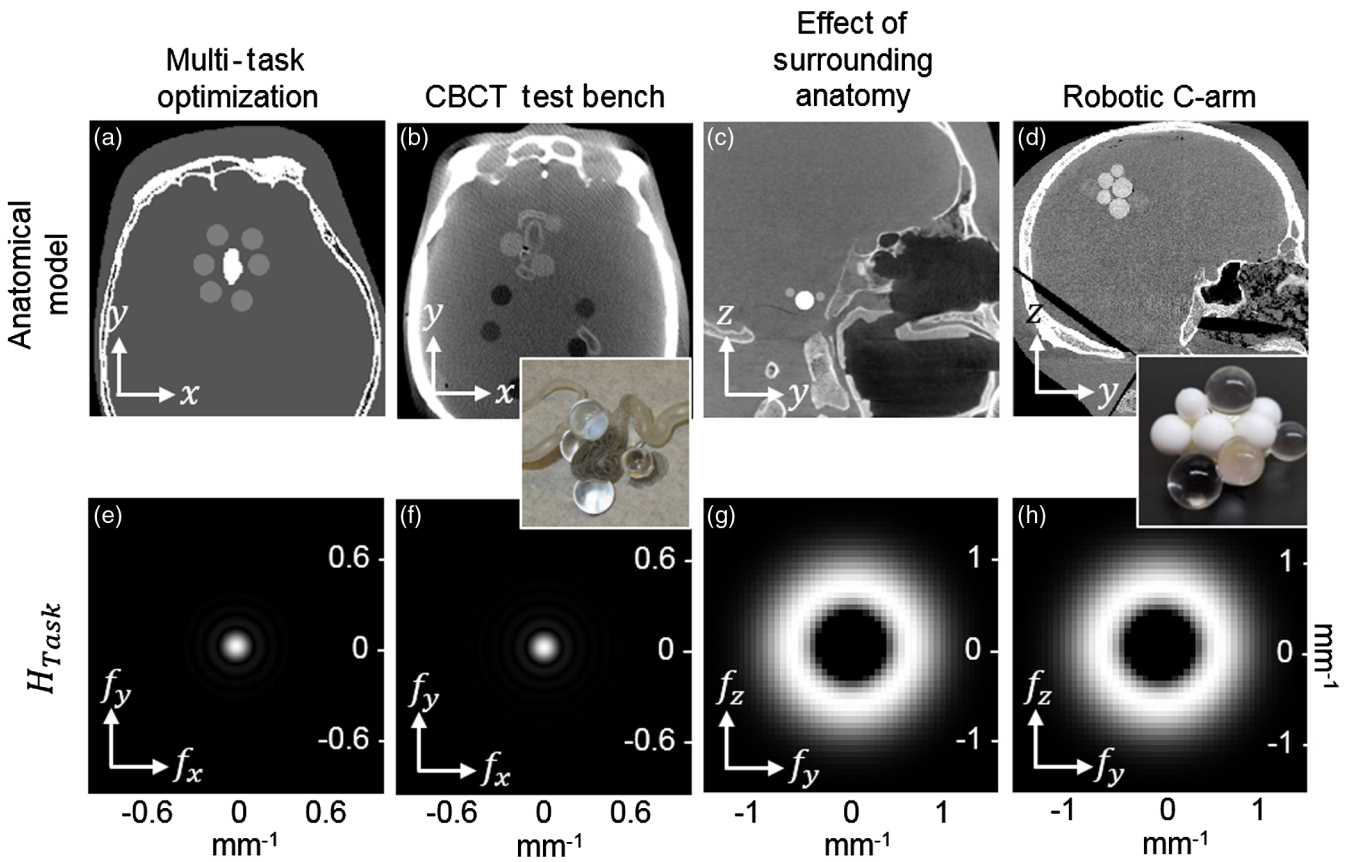

Fig. 3 Summary of experiments testing task-driven imaging in neuroradiology. (a) Simulation of the postoperative assessment of an embolization coil using the multilocation optimization to detect the surrounding hemorrhage. (b) Visualization of hemorrhage near an embolization coil using a CBCT test bench. (c) Simulation of an AVM at various locations in the cranium to observe the effect of surrounding anatomy on the optimal orbit. (d) An AVM model created in an anthropomorphic head phantom to demonstrate the full workflow of task-driven imaging on a robotic C-arm. (e)–(h) The task functions, $H_{\text{Task}(j)}$, used in experiments (a)–(d), respectively.

volume. The intracranial aneurysm was then instrumented with a stent and platinum embolization coils by an interventional radiologist under fluoroscopic guidance until the vessel was sufficiently full. The phantom was then scanned according to the protocols described in Sec. 3.1 to compare the task-driven orbit with a standard circular trajectory.

The optimal trajectory was solved using a multilocation, maxi-min objective for three locations posterior to the embolization coil with the task function shown in Fig. 3(f) describing detection of the low-frequency, low-contrast hemorrhage [identical to the task function described in Sec. 3.2 and as shown in Fig. 3(e)]. The optimal trajectory was computed using a parameterized orbit of 29 periodic basis functions to allow a higher degree of flexibility in the orbit and constrained within $\pm 30°$ tilt to account for physical constraints of the test bench experimental setup. The on-the-fly computation approach and the same CMA-ES optimization parameters as in Sec. 3.2 were used. As described in Sec. 3.1, the 364 nearest vertices from the projection data acquired over the full range in θ and ϕ were selected for the task-driven orbit. Image reconstruction for both the task-driven orbit and the reference circular orbit used the quadratic PL algorithm with the same parameters as in Sec. 3.2, except the regularization parameter β was increased slightly to 7×10^5 to account for the differences in the fluence levels.

3.4 *Effect of Surrounding Anatomy*

A similar simulation was performed to examine the effect of the location of the stimulus within the cranium on the optimal task-driven trajectory—in this case, embolization of an AVM using a highly attenuating polymeric glue.[10] Postoperative assessment of AVM embolization includes localizing untreated regions of the AVM nidus. This experiment used a digital anthropomorphic head phantom, as illustrated in Fig. 3(c), locating a simulated AVM in the skull base, the lateral cranium, or the crown of the skull. The central core of the AVM after embolization was represented by a sphere of diameter 10 mm with $\mu = 1.0$ mm^{-1} to represent a nidus of vessels filled with high-contrast glue. Six 5-mm diameter low-contrast spheres were placed around the central core with a contrast of 0.005 mm^{-1} compared to the soft-tissue background to represent potential untreated sites. The simulation mimicked the robotic C-arm system geometry with bare-beam fluence set to 10^4 photons per detector element to match the exposure of the robotic C-arm system. A monoenergetic forward model with added Poisson noise was used to generate 360 projection images over 360 deg.

Six midfrequency imaging tasks were defined at the location of each simulated untreated site for the multitask optimization using the maxi-min objective [Fig. 3(g)]. In this experiment midfrequencies were emphasized to capture the task of

distinguishing a small vessel adjacent to the AVM nidus. This experiment used the precomputation approach described in Ref. 3 to utilize the second proposed method. Although more accurate in calculating the MTF and NPS, the precomputation approach is memory-intensive, thereby limiting the total number of imaging tasks. To make use of the second proposed parameterization of the source trajectory described in Ref. 3, B-spline basis functions were used with eight equally spaced knots, and the trajectories were constrained to tilt angles in the range of $\phi = -30$ deg to $+30$ deg and rotation angles of $\theta = 1$ deg to 360 deg to match the extent of the robotic C-arm system. As trajectories from B-spline basis functions have increased flexibility over periodic basis functions, the CMA-ES optimization algorithm was used to estimate $\hat{\Omega}$ using a population size of 200 with six restarts and random uniform initialization.

Quadratic PL reconstructions for the optimal trajectory and a circular trajectory (generated with the same bare-beam fluence and number of projections) were performed using 200 iterations with 10 subsets to stabilize convergence during reconstruction and regularization strength $\beta = 10^5$, again to balance the noise with resolution at the task location. Images were reconstructed with $512 \times 512 \times 512$ voxels and 0.5-mm isotropic voxel size.

3.5 *Task-Driven Imaging on a Robotic C-Arm*

The full task-driven imaging framework was tested on the robotic C-arm using an AVM model within an anthropomorphic head phantom (The Phantom Laboratory, Greenwich, New York), similar to that described in Sec. 3.3 and illustrated in Fig. 3(d). The brain-like background was the same as in Sec. 3.3 ($\mu = 0.0188$ mm^{-1}) and the AVM model was created by clustering ten Teflon spheres ($\mu = 0.03$ mm^{-1}) and six acrylic spheres ($\mu = 0.0195$ mm^{-1}) ranging in diameter from 5 to 15 mm at the crown of the skull. A prior image was obtained on a CBCT test bench and registered to the robotic C-arm geometry. Six imaging tasks were defined at the edges between the Teflon and acrylic spheres, presenting a midfrequency task function with a contrast of 0.0007 mm^{-1}, as shown in Fig. 3(h) (similar to the task described in Sec. 3.4). Orbit optimization was performed in the same manner as in Sec. 3.4 using the precomputation approach.

The phantom was subsequently imaged on the robotic C-arm operated in the step-and-shoot mode to move through the optimal task-driven orbit (360 projections at a fixed technique of 102 kV and 0.18 mAs/projection). Quadratic PL reconstruction was again performed using 200 iterations with 10 subsets and 0.5-mm isotropic voxels on a $700 \times 700 \times 700$ voxel grid, with β lowered to $10^{3.5}$ to increase the resolution at the task location. For comparison with a standard circular orbit, a low-dose research scan protocol was used (496 projections over a 200-deg circular orbit with the same technique as above). A total of 360 approximately equally spaced projections were used for reconstruction. The same PL parameters were applied for image reconstruction for both the task-driven and the circular orbits.

4 Results

4.1 *Multitask Optimization*

Results of the embolization coil imaging experiment are summarized in Fig. 4. The optimization sought the maxi-min solution for detectability of hemorrhage over an ensemble of locations [Fig. 4(a)] surrounding an embolization coil. Compared to a conventional circular orbit, the resulting task-driven orbit exhibits a tilt and low-frequency excursions from a plane, as shown in Fig. 4(b). The orbit is clipped at two positions due to the ± 50-deg collision constraint. Figure 4(c) shows the maps of fluence through 6 of the 30 stimulus locations for all possible source rotations/tilts. These maps illustrate the importance of data fidelity in selecting a particular orbit. Both the task-driven orbit (pink) and conventional circular orbit (green horizontal line) are shown superimposed on the fluence maps, showing that the fluence through each stimulus depends on

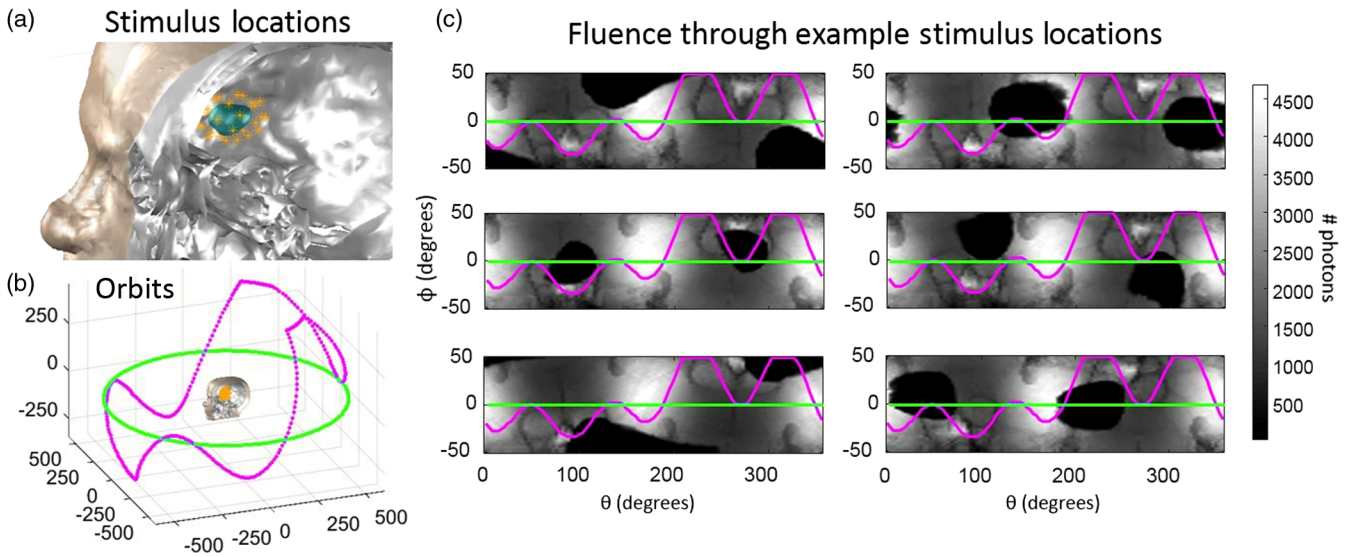

Fig. 4 Task-driven orbit design for imaging around an embolization coil. (a) A total of 30 locations (orange markers) in proximity to the embolization coil mark the locations at which detectability of hemorrhage is computed in iterative optimization. (b) The task-driven (pink) and standard circular (green) orbits. (c) Orbits (θ, ϕ) superimposed on maps showing the fluence passing through 6 of the 30 stimulus locations.

location with respect to the surrounding anatomy and the embolization coil. The task-driven orbit tends to vertices that avoid the strong attenuation of the embolization coil (evident as a "black hole" in the fluence maps through which few x-rays are transmitted) and appears to exercise an orbit involving fewer redundant view angles over the 360-deg orbit, i.e., if rays pass through the coil on one side of the trajectory, a tilt is sought for the opposing view to avoid the coil. While it is not possible to completely avoid rays passing through the coil for all stimulus locations, redundancy in the orbit allows collection of asymmetric views to compensate low-fidelity data in the opposing view.

CBCT images reconstructed from the circular and task-driven orbits are shown in Fig. 5. Images for the circular orbit are degraded severely in proximity to the embolization coil due to decreased data fidelity (high attenuation) for measurements passing through the coil. Note that this degradation is entirely due to the measurement statistics (noise), as the simulation in this study did not include polyenergetic effects. Strongly correlated noise (streaks) around the coil obscures many of the stimuli. By contrast, the task-driven orbit improves the visualization of the simulated hemorrhages, and while high-frequency noise is elevated at other locations in the head (attributed to view sampling effects), the streaks and shading at the specified locations of interest are markedly reduced. The multi-task design objective facilitates improved image quality at all locations around the embolization coil, effectively pushing the image quality degradations away from the task locations.

4.2 *Task-Driven Imaging in Real Data (CBCT Test Bench)*

Figure 6 summarizes the test bench experiment involving an embolization coil in an anthropomorphic phantom. The top row of images (acquired before delivery of the coil) shows the locations of the simulated spherical hemorrhage. For this experiment, the task-driven orbit design focuses on maximizing the detectability at three locations posterior to the aneurysm. The shape of the designed orbit exhibits interesting features including an overall tilt to the orbit—selecting projections that avoid alignment of the highly attenuating skull base with the target region of interest. In addition, the task-driven orbit appears to seek nonredundant views with a slight wobble in the orbit.

For a scan comprising 364 projection views over 360 deg, the air kerma is $D_w \sim 21.1$ mGy, recognizing that the dose for a task-driven orbit (with oblique views up to 30 deg off the central axial plane) likely departs somewhat from the dose for a circular scan. To the extent that the projection views are equally distributed above and below the central axial plane, the difference in dose is believed to be small.

Images from a standard circular orbit exhibit poor visualization in the region of interest, and both the posterior hemorrhage and the legs of the stent used to hold the embolization coil in place are obscured by streaking and blooming effects due to the low-fidelity measurements through the coil. By contrast, the task-driven trajectory shows good visualization of the posterior bleed as well as the legs of the stent. Residual contrast agent in the simulated vasculature is also evident (whereas the preoperative scan shows only the lumen of the simulated vessel). As the task-driven optimization specified the posterior hemorrhage as the imaging task, it did not improve the image quality anterior to the coil. In addition, although the performance prediction and system model ignored polyenergetic effects, the models were sufficiently accurate to identify an orbit yielding measurable improvement in image quality.

4.3 *Effect of Surrounding Anatomy*

Figure 7 shows the fluence maps, task-driven trajectories, and reconstructed images of a simulated AVM—with the goal of optimizing detectability for six locations around the high-contrast embolization of an AVM nidus—in the skull base, the lateral cranial vault, or the interior crown of the skull. The task-driven approach solved the maxi-min objective for each region, as shown in Figs. 7(a)–7(c). Fluence maps are shown for stimuli that exhibited the greatest increase in detectability. Analogous to the embolization coil in Sec. 4.1, the embolized AVM strongly influences the fluence maps in each region, but the fluence maps differ for each location due to the differences in surrounding anatomy—influencing the overall attenuation so as to drive the solution to a distinct optimal orbit for different locations in the head. This demonstrates that knowledge of both the

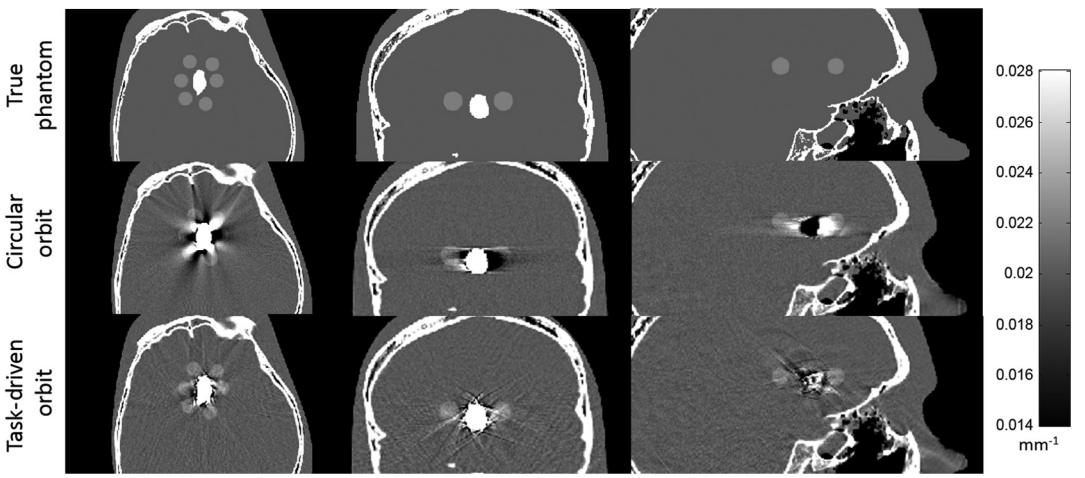

Fig. 5 Task-driven imaging of simulated hemorrhage around an embolization coil. The circular orbit results in strong photon starvation artifacts/noise in proximity to the coil. The task-driven orbit mitigates such effects and improves the conspicuity of simulated lesions near the coil.

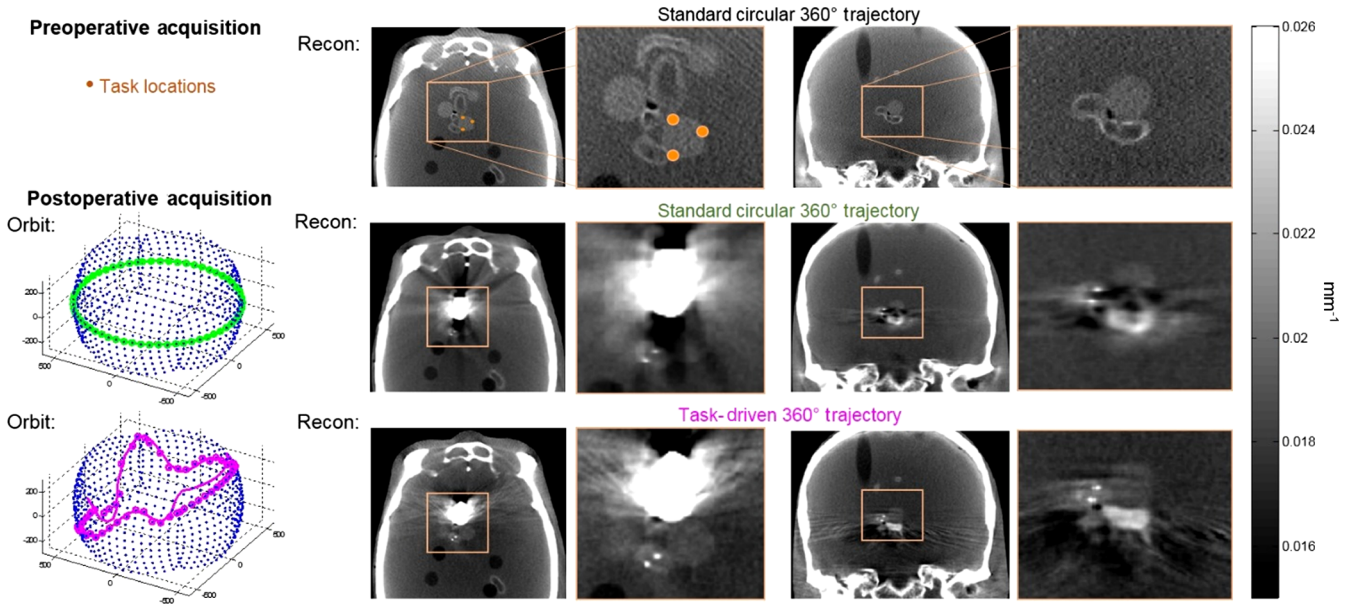

Fig. 6 Task-driven orbit applied on the CBCT test bench for visualization of hemorrhage posterior to a coiled aneurysm. The preoperative scan shows details of the vessel and simulated spherical bleeds adjacent to an aneurysm. Three stimulus locations were selected posterior to the aneurysm. Following placement of the coil, a standard circular orbit exhibits severe shading and streaks that confound visualization about the embolization coil. The task-driven orbit yields improved visualization of both the posterior bleed and stent and the residual contrast agent in the vasculature.

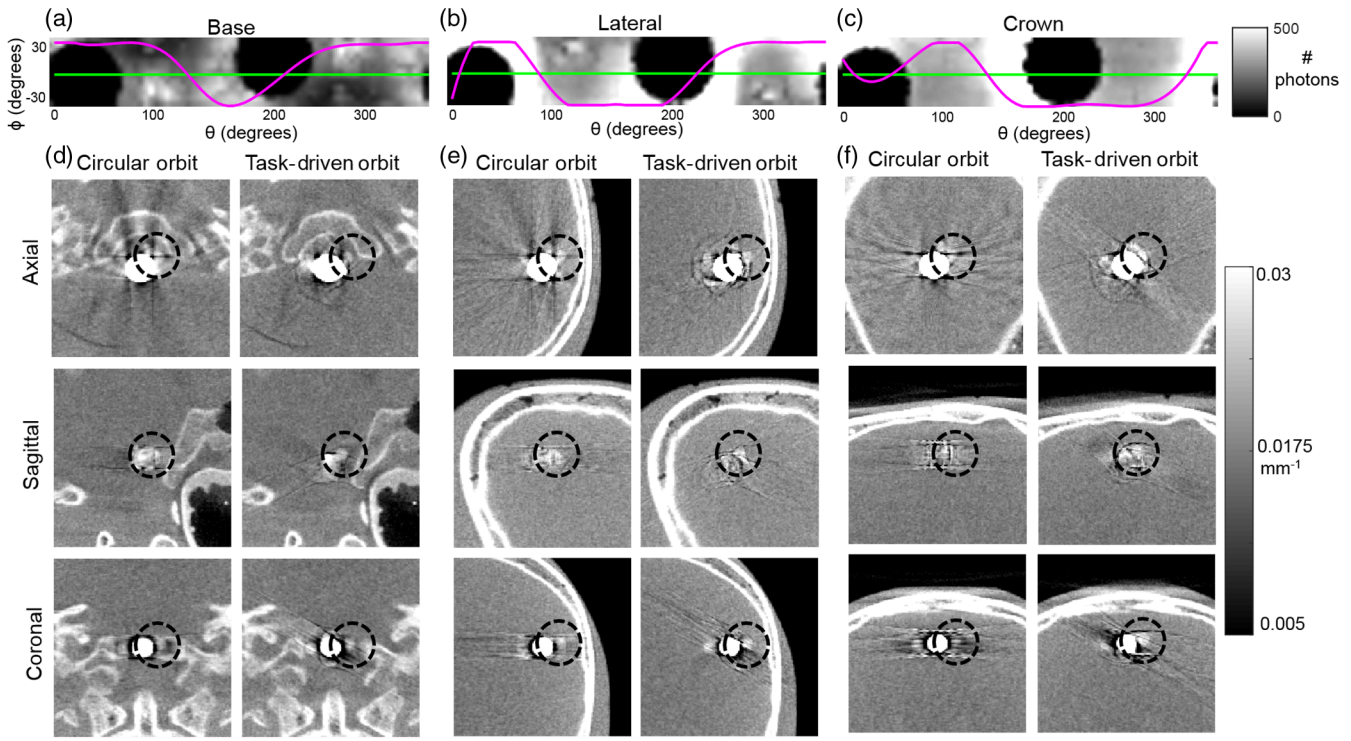

Fig. 7 Task-driven imaging of a simulated AVM at the skull base, lateral cranium, and crown using six imaging tasks surrounding the AVM. Fluence maps in (a)–(c) show that the task-driven orbit seeks a path yielding highest fluence through the location of interest. Reconstructed images in (d)–(f) show slices through the spherical stimulus exhibiting the greatest increase in d'.

surrounding anatomy and the location of interest for the imaging task(s) are necessary for trajectory optimization.

CBCT reconstructions at the stimulus exhibiting the greatest increase in d' are shown in Figs. 7(d)–7(f), comparing the results of a circular orbit with the results of the task-driven orbits. The spherical stimulus is more conspicuous in the task-driven images due to a reduction and/or reorientation of streaking and blooming effects arising from the high-contrast

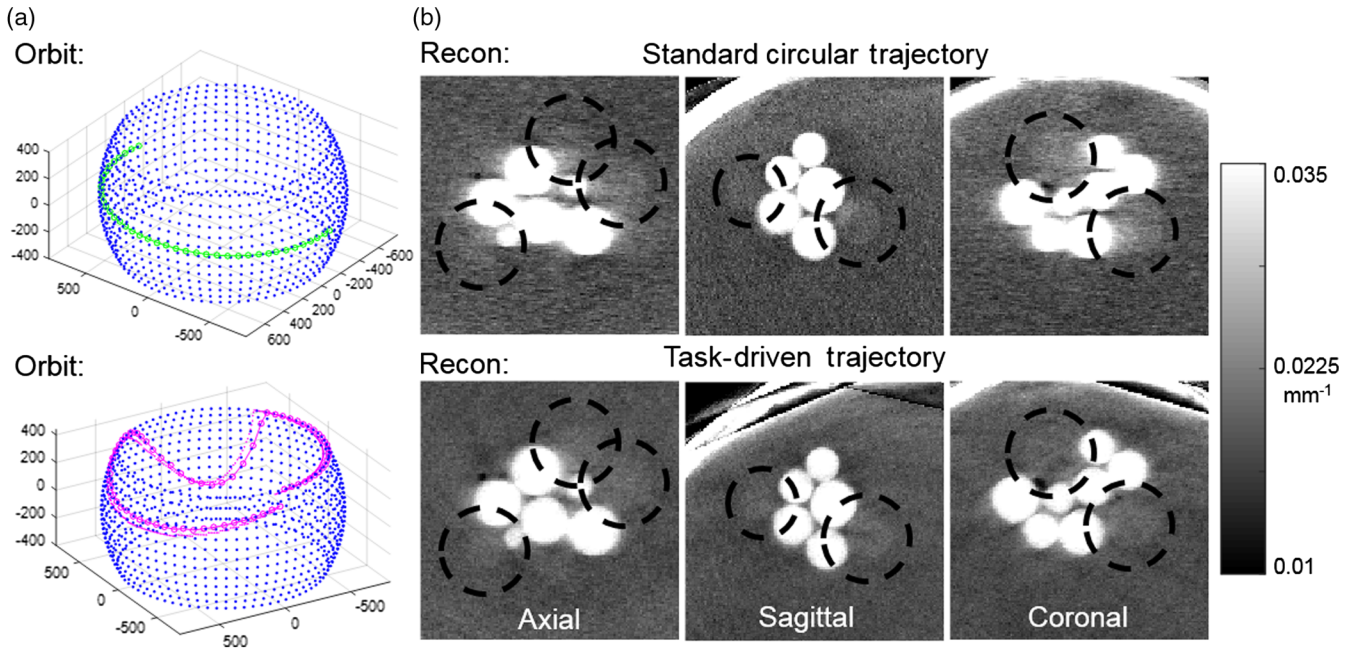

Fig. 8 An AVM imaged on the robotic C-arm using circular and task-driven trajectories. (a) Illustration of the circular and task-driven orbits (green and pink, respectively). (b) CBCT reconstructions for each orbit, showing improved visualization of low-contrast spheres (highlighted by black dashed circles). The task-driven orbit exhibits reduced blurring of sphere edges, most noticeably in the axial and coronal planes.

AVM embolization. Detectability for tasks at the skull base improved on average by 20.2%, at the lateral cranium on average by 28.6%, and at the crown on average by 7.0%. The smaller increase in d' at the crown is due to the fact that there is little room for improvement in a region for which rays traversing the stimulus is already low.

4.4 *Task-Driven Imaging on a Robotic C-Arm*

The AVM model imaged on the robotic C-arm is shown in Fig. 8. The task-driven trajectory used a maxi-min objective over the six task locations, as shown in Fig. 8(a), giving an increase in d' at all locations compared to a circular orbit. The lowest increase in d' is 7.0%, and the greatest increase is 13.0%, with an average increase of 10.3%. As illustrated in Fig. 8(a), the task-driven orbit favors large, positive tilt angles, with an excursion at $\theta = 170$ deg that provides higher fidelity (lower attenuation) lateral views. Continuity of the scan orbit is ensured by the underlying B-spline model, but there is no constraint that the C-arm pose should match at the start ($\theta = 0$ deg) and stop ($\theta = 360$ deg) locations, which explains the observed discontinuity at the endpoints of the orbit. As shown in Ref. 3, this increased flexibility can, in certain cases, be advantageous in orbit design.

The air kerma was measured, as described in Sec. 3.1, for a low-dose research protocol with a circular orbit and 360 projections over 200 deg, giving a value of $D_w \sim 9.0$ mGy, recognizing that the dose for a task-driven scan may differ from that of a circular scan due to the oblique views and differences in attenuation by the table.

The images in Fig. 8(b) show a slight improvement in visibility of the acrylic spheres for the task-driven images in the axial, sagittal, and coronal images.

5 Discussion

This work builds on the theoretical framework detailed in the companion paper[3] to investigate particular imaging scenarios in interventional neuroradiology, e.g., detection of hemorrhage in proximity to a coiled aneurysm and detection of untreated regions within an AVM nidus. The results demonstrate improvements in detectability index for task-driven orbits, with visible improvements in both simulated and real CBCT images. The optimized orbits generally sought the highest fidelity (lowest attenuation) views and tended toward asymmetric vertices to reduce data redundancy in a 360-deg orbit. In the task-driven orbit, vertices separated by 180 deg are oblique relative to one another so that a lower fidelity view in the first half of the orbit may be compensated in the second half of the orbit. The task-driven orbits result in an improved visualization of intracranial hemorrhage due to reduced noise and improved sampling in the region of interest and by the distribution of streak artifacts to interfere less with detection of the stimuli. We have also investigated the effect of stimulus location and surrounding anatomy on trajectory design for different sites within the cranium. Our experimental studies suggest that the surrounding cranial anatomy can affect the optimal orbit, showing the sensitivity of the optimization to both the anatomy and the instrumentation or implants.

In addition, this work demonstrated the operation of a clinical robotic C-arm for task-driven imaging by moving it through an optimal, noncircular orbit designed to improve the performance of the imaging tasks. A complex, task-driven orbit was demonstrated in a realistic clinical scenario, encompassing calculation of the task-driven orbit from a prior CBCT image, transferal of the trajectory to the robotic C-arm, acquisition of a noncircular orbit, geometric calibration of the noncircular orbit using a self-calibration technique, and reconstruction of the 3-D image using model-based iterative reconstruction.

For this scenario, the effect of regularization in model-based image reconstruction was apparent in the final images; because the circular orbit involved lower fidelity projection data, the regularization was increased accordingly, causing increased blur of the sphere edges. The task-driven orbit, on the other hand, gathered higher-fidelity projection data and was less reliant on the regularization to mitigate noise, yielding clearer delineation of the sphere edges. These results demonstrated the first successful implementation of task-driven imaging on a real clinical system for a semirealistic anatomical context and imaging task.

The experiments demonstrated here perform optimization over a small number of task functions limited to a small region of the cranium using the maxi-min objective function, which ensures that imaging performance is not sacrificed in some locations in favor of others, recognizing that there may very well be situations for which a different multilocation objective is a better choice. It may also be of interest to perform the optimization over larger regions by including task locations farther from the attenuating object to give more uniform image quality over a larger volume of interest. In theory, one could define locations throughout the entire cranial vault as locations of interest to generate an orbit that provides globally increased detectability. In addition, imaging tasks of various frequency content and contrast could be included in the optimization to allow further uncertainty in the stimulus.

An important point of future work is the expansion of parameters contained within the optimization to further improve the orbit and overall imaging chain—for example, scan technique factors (kV and mAs) and reconstruction parameters (regularization constant β). Such a task-driven CBCT scanning process presents an ambitious new paradigm for prospective optimization of image quality and/or reduction in the patient dose. For flexible imaging platforms such as a robotic C-arm, additional DoFs could be incorporated in defining the source–detector trajectory beyond the two (θ, ϕ) investigated in the results reported above—for example, translation of the source and/or detector for nonisocentric orbits with large FOV.

In this work, we imposed constraints on the tilt angle to conserve collision limits and required a 360 deg total orbit in all cases. Changing or removing these constraints may be of interest to optimal short-scan trajectories and extension of task-driven imaging to tomosynthesis in which the optimal set of limited projection data is solved for difficult imaging scenarios. We also constrained B-spline knot locations to be equally spaced along the trajectory, recognizing that this sampling interval may not necessarily be optimal. This represents another parameter that could be optimized, for example, by having a higher sampling density of knots for views carrying spatial frequency content consistent with the imaging task.

In the experiments presented, the anatomical model was an exact representation of the object and did not consider potential uncertainty. In realistic clinical scenarios, there may be extraneous regions of high attenuation within the patient stemming from surgical tools, contrast agent, unplanned embolization sites, etc. that were not accounted for in the anatomical model of the patient. This presents a limitation that could be explored further, for example, by using probability distributions for the patient model and parameters defining the imaging tasks. This would result in a distribution of orbits from which a robust estimate of the ensemble optimum could be chosen.

Another limitation of relying on an anatomical model is the image quality of μ_{prior}. We envision that—depending on clinical workflow—the source of μ_{prior} could be a diagnostic-quality MDCT acquired prior to a procedure or a CBCT acquired at the beginning of the procedure. The latter raises potential limitations in instances of strong truncation, which introduces error in the forward model in the optimization. T1- or T2-weighted MRI is typically not a useful input model, but numerous methods for synthesizing a CT-like image (i.e., an image with intensities proportional to electron density) from MRI have emerged in the past decade.

The current work compares the image quality in task-driven and conventional circular orbits under conditions of matched bare-beam exposure. Dosimetry (e.g., D_w measurements) for task-driven orbits introduces some complexity associated with oblique projections and is difficult to prescribe for cases in which the orbit is not known *a priori*. Such considerations raise interesting future work in dosimetry for noncircular orbits, including measurement and Monte Carlo methods.

Further testing of task-driven imaging methods would benefit from a more streamlined interface for executing noncircular orbits on the robotic C-arm. In the current work, noncircular orbits were realized using a step-and-shoot method by directing the robot to each vertex via an external workstation. Images were acquired using a 2-D radiographic imaging protocol at each vertex, collected individually, and processed offline. This fairly time-consuming workflow is not suitable for clinical studies and would be greatly improved by an interface allowing 3-D imaging protocols with orbit and vertex definition consistent with smooth, continuous motion of the robot.

Overall, task-driven orbits appear to be of most benefit in difficult imaging scenarios in which highly attenuating objects in the FOV would cause strong streaks and other metal artifacts that would confound visualization of nearby, low-contrast objects. This is a common scenario in IGIs where CBCT images taken during the procedure often include metal instrumentation, and the regions of interest tend to be in proximity to such instrumentation. Application of task-driven imaging in scenarios beyond neuroradiology may be of similar benefit—for example, orthopedic imaging, dental imaging, and musculoskeletal imaging, where metal implants are a common source of image artifacts and reduced image quality. Task-driven orbits offer the potential to improve image quality in the interventional theater, a new approach to dose reduction, and a potentially more reliable check against complications in the operating room.

Disclosures

No conflicts of interest, financial or otherwise, are declared by the authors.

Acknowledgments

This research was supported by the National Institutes of Health Grant Nos. R01-EB-017226 and U01-EB-018758, academic-industry partnership with Siemens Healthineers (AX Division, Forcheim, Germany), and a Johns Hopkins University Catalyst Grant. The authors wish to thank Robin Belcher (Department of Radiology, Johns Hopkins University), Robert Meyer (Siemens Medical Solutions USA, Inc., Customer Solutions Group, Baltimore/Washington DC), and Sebastian Schafer (Siemens Healthineers, AX Division) for their assistance with the robotic C-arm imaging system and Tilley II, Zhao, and Radvani (Johns Hopkins University) for their help with experimentation.

References

1. J. A. Carrino et al., "Dedicated cone-beam CT system for extremity imaging," *Radiology* **270**(3), 816–824 (2013).
2. T. Berris, R. Gupta, and M. M. Rehani, "Radiation dose from cone-beam CT in neuroradiology applications," *Am. J. Roentgenol.* **200**(4), 755–761 (2013).
3. J. W. Stayman et al., "Task-driven source–detector trajectories in cone-beam computed tomography: I. Theory and methods," *J. Med. Imaging* **6**(2), 025002 (2019).
4. J. W. Stayman, G. J. Gang, and J. H. Siewerdsen, "Task-based optimization of source-detector orbits in interventional cone-beam CT," in *Proc. Int. Meet. Fully Three-Dimensional Image Reconstruct. in Radiol. and Nucl. Med.* (2015).
5. G. J. Gang et al., "Task-driven image acquisition and reconstruction in cone-beam CT," *Phys. Med. Biol.* **60**(8), 3129–3150 (2015).
6. H. Dang et al., "Task-based statistical image reconstruction for high-quality cone-beam CT," *Phys. Med. Biol.* **62**(22), 8693–8719 (2017).
7. S. Ouadah et al., "Task-driven orbit design and implementation on a robotic C-arm system for cone-beam CT," *Proc. SPIE* **10132**, 101320H (2017).
8. A. C. Miracle and S. K. Mukherji, "Cone beam CT of the head and neck, part 2: clinical applications," *Am. J. Neuroradiol.* **30**(7), 1285–1292 (2009).
9. F. Alabdulghani, A. O'Brien, and D. Brophy, "Application of cone-beam computed tomography angiography in a uterine fibroid embolization procedure: a case report," *Radiol. Case Rep.* **13**(1), 130–134 (2018).
10. J. J. Leyon et al., "Endovascular embolization: review of currently available embolization agents," *Curr. Prob. Diagn. Radiol.* **43**(1), 35–53 (2014).
11. A. Uneri et al., "3D–2D registration for surgical guidance: effect of projection view angles on registration accuracy," *Phys. Med. Biol.* **59**(2), 271–287 (2014).
12. F. Noo et al., "Analytic method based on identification of ellipse parameters for scanner calibration in cone-beam tomography," *Phys. Med. Biol.* **45**, 3489–3508 (2000).
13. Y. Cho et al., "Accurate technique for complete geometric calibration of cone-beam computed tomography systems," *Med. Phys.* **32**(4), 968–983 (2005).
14. C. Mennessier, R. Clackdoyle, and F. Noo, "Direct determination of geometric alignment parameters for cone-beam scanners," *Phys. Med. Biol.* **54**, 1633–1660 (2009).
15. S. Ouadah et al., "Self-calibration of cone-beam CT geometry using 3D-2D image registration," *Phys. Med. Biol.* **61**(7), 2613–2632 (2016).
16. G. J. Gang, J. H. Siewerdsen, and J. W. Stayman, "Task-driven optimization of CT tube current modulation and regularization in model-based iterative reconstruction," *Phys. Med. Biol.* **62**(12), 4777–4797 (2017).
17. H. Dang, J. H. Siewerdsen, and J. W. Stayman, "Prospective regularization design in prior-image-based reconstruction," *Phys. Med. Biol.* **60**(24), 9515–9536 (2015).
18. J. W. Stayman and J. A. Fessler, "Regularization for uniform spatial resolution properties in penalized-likelihood image reconstruction," *IEEE Trans. Med. Imaging* **19**(6), 601–615 (2000).
19. N. Hansen, *The CMA Evolution Strategy: A Comparing Review Towards a New Evolutionary Computation*, Springer, Berlin, pp 75–102 (2006).
20. Y. Otake et al., "Robust 3D–2D image registration: application to spine interventions and vertebral labeling in the presence of anatomical deformation," *Phys. Med. Biol.* **58**(23), 8535–8553 (2013).
21. R. Fahrig et al., "Dose and image quality for a cone-beam C-arm CT system," *Med. Phys.* **33**(12), 4541–4550 (2006).
22. M. J. Daly et al., "Intraoperative cone-beam CT for guidance of head and neck surgery: Assessment of dose and image quality using a C-arm prototype," *Med. Phys.* **33**(10), 3767–3780 (2006).

Biographies of the authors are not available.